ACS APPLIED MATERIALS & INTERFACES

Research Article

www.acsami.org

Hybrid Organotin and Tin Oxide-based Thin Films Processed from Alkynylorganotins: Synthesis, Characterization, and Gas Sensing Properties.

Laetitia Renard,[†] Joachim Brötz,[‡] Hartmut Fuess,[‡] Aleksander Gurlo,[‡] Ralf Riedel,[‡] and Thierry Toupance*,[†]

[†]University of Bordeaux, Institut des Sciences Moléculaires, UMR 5255 CNRS, 351 Cours de la Libération, F-33405 Talence Cedex, France

[‡]Fachbereich Material- und Geowissenshaften, Technische Universität Darmstadt, Petersenstrasse 23, D-64287 Darmstadt, Germany

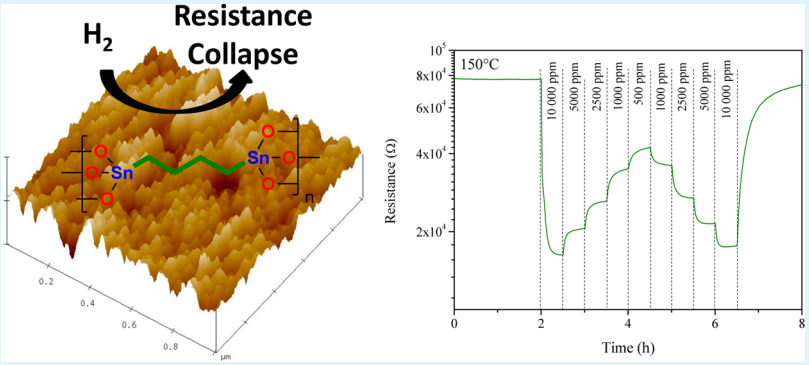

ABSTRACT: Hydrolysis−condensation of bis(triprop-1-ynylstannyl)butylene led to nanostructured bridged polystannoxane films yielding tin dioxide thin layers upon UV-treatment or annealing in air. According to Fourier transform infrared (FTIR) spectroscopy, contact angle measurements, X-ray diffraction (XRD), X-ray photoelectron spectroscopy (XPS), atomic force microscopy (AFM), and scanning electron microscopy (SEM) data, the films were composed of a network of aggregated "pseudo-particles", as calcination at 600 °C is required to form cassiterite nanocrystalline SnO_2 particles. In the presence of reductive gases such as H_2 and CO, these films gave rise to highly sensitive, reversible, and reproducible responses. The best selectivity toward H_2 was reached at 150 °C with the hybrid thin films that do not show any response to CO at 20−200 °C. On the other hand, the SnO_2 films prepared at 600 °C are more sensitive to H_2 than to CO with best operating temperature in the 300−350 °C range. This organometallic approach provides an entirely new class of gas-sensing materials based on a class II organic−inorganic hybrid layer, along with a new way to include organic functionality in gas sensing metal oxides.

KEYWORDS: *organotins, organic−inorganic hybrid materials, tin dioxide, thin films, gas sensors*

INTRODUCTION

Over the past two decades, nanostructured wide-bandgap semiconductor metal oxides (SMOs) have attracted much attention owing to their remarkable chemical, electrical, electrochemical and optical properties outperforming their bulk counterparts and, also, due to their potential applications in nanodevices. For instance, tin dioxide (SnO_2), an environmentally friendly wide gap n-type SMO with a direct band gap (E_g = 3.6 eV at 300 K), has been extensively studied as a promising multifunctional material for a wide range of applications such as porous support in heterogeneous catalysis,[1,2] photocatalyst to decompose undesirable organics,[3,4] transparent conductive electrode in optoelectronic devices,[5] semiconductor in transistors,[6,7] electrode material for lithium ion batteries[8−10] or supercapacitors,[11,12] and porous semiconducting photoanode in dye-sensitized solar cells.[13−15] Furthermore, SnO_2 is widely used in the fabrication of commercial SMO-based sensors and is the best-understood prototype in fundamental studies of gas sensing mechanisms.[16−19] Even though the precise sensing mechanism is still under active debate,[20−23] the detection process is strongly connected to the reversible gas adsorption−desorption phenomena at the SnO_2 surface that induce charge transfer process between the SMO and the adsorbates. The concentration in charge carriers is thus modified by the adsorbed species; a reductive atmosphere causes a conductance increase, while an oxidative atmosphere provokes a conductance decrease. Various reducing (e.g., CO,[24−26] H_2,[27] CH_4,[28] or alcohols[29]) and oxidizing (e.g., NO_2)[30] gases are detected by SnO_2-based sensors. Commercial SnO_2-based

Received: July 18, 2014
Accepted: September 5, 2014
Published: September 5, 2014

sensors usually involve several hundred nm to several μm polycrystalline thick layers, their performance is strongly influenced by various parameters including the structural properties of SnO_2 particles and the porosity and thickness of sensing layers. The enhancement of the sensing performance necessitates small well-crystallized SnO_2 particles with a large surface-to-volume ratio and a suitable layer porosity for good diffusion of gaseous species. In this context, the gas-sensing properties of well-defined SnO_2 materials in the form of monodispersed nanoparticles,[31−33] nanorods,[34,35] nanowires,[36−38] nanobelts,[39] nanoboxes,[40,41] nanoflowers,[42] hollow spheres[43] and inverse opals,[44,45] have been intensively studied.[46] Some of these architectures have been processed as rather thick layers that result in promising gas sensing properties. Recent studies have also evidenced that a careful control of the morphology of SnO_2 crystals significantly influences their gas sensing activity.[47−50] On the other hand, fewer studies have been devoted to thin layer technology for gas sensors, even though this technology could be applied in microelectronic devices to diminish costs and power consumption. Various techniques, such as reactive magnetron sputtering,[51,52] evaporation,[53] chemical vapor deposition,[54,55] and spray pyrolysis,[56,57] have been employed to elaborate SnO_2 thin films yielding dense layers. Furthermore, the self-[58] or surfactant templating[59] approaches associating the sol−gel processing and the dip-coating deposition technique have been developed to yield mesoporous tin dioxide layers with finely tuned porosity. Nonetheless, the resulting active layers suffer from some limitations of gas sensing applications due to small crystallite size. Organometallic and metallo-organic alkoxide precursors have also been introduced to fabricate SnO_2 thin films via the chemical vapor deposition or the sol−gel process technique,[60] but some difficulties have arisen from the incomplete oxidation of a mixture of phases.[61] Recently, we have set up a new organometallic solution route toward functional tin-based hybrid materials based on the design of suitable alkynyltin compounds as sol−gel precursors, because the elimination of the organic component provides tin oxides. Thus, self-assembled organotin-based hybrid powders[62] and thin films[63] could be readily prepared from organically bridged ditin hexaalkynides.[64] Futhermore, nanoporous organotin-based hybrid thin films showed unexpected selectivity for hydrogen gas sensing at moderate temperature.[63]

In this context, we herein report on the preparation and the gas sensing properties of thin nanocrystalline SnO_2 layers through post-treatment of a spin-coated organotin-based hybrid thin film obtained by hydrolysis and condensation of 1,4-bis(triprop-1-ynylstannyl)butane (Scheme 1). A careful tuning of the post-treatment conditions (i.e., UV-irradiation at room temperature or calcination in air), has enabled us to control the structure and morphology of SnO_2 films for gas detection (Table 1). Yielding excellent sensitivity toward hydrogen (H_2) and carbon monoxide (CO), this film processing method was very simple and straightforward because it required neither additives as surfactant nor prior synthesis of tin dioxide nanostructures.

Scheme 1. Chemical Formula of 1,4-Bis(triprop-1-ynylstannyl)butane

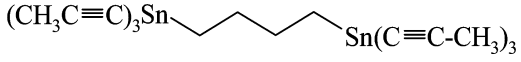

Table 1. Post-Treatment Conditions and Characteristics of the Various Samples Studied in This Paper

sample	aging/annealing temperature (°C)	phase composition	sensing performance
TF^{120}	120	amorphous butylene-based hybrid	sensitive to H_2
TF^{500}	500	amorphous oxide	sensitive to H_2 and CO
TF^{600}	600	nanocrystalline oxide	sensitive to H_2 and CO
TF^{UV}	UV	amorphous oxide	not sensitive

EXPERIMENTAL SECTION

General. Tetrahydrofuran (THF; Fisher) was purified by distillation over Na/benzophenone prior to use. 1,4-Bis(triprop-1-ynylstannyl)butane was prepared following a previously reported procedure:[64] A 2.5 M solution of BuLi (21.24 mL, 53.10 mmol) was added to a solution of propyne (3.44 mL, 60.69 mmol) in toluene (50 mL) in a 250 mL three-necked flask at −78 °C. After the solution stirred for 15 min, a solution of 1,4-bis(trichlorotin)butane (3.8 g, 7.59 mmol) in 40 mL of toluene was added at −78 °C. After stirring for 15 h at 70 °C, the suspension was filtered over dry $MgSO_4$, and the solvent was evaporated under vacuum to give the expected compound as a white solid (yield, 85%).

Glass slide (1 × 1 cm) or Si(100) wafer (ITME) substrates were cleaned just before use. They were treated with hot chloroform (analytical grade, Aldrich) for 15 min and then exposed to UV−ozone (homemade apparatus, λ = 185−254 nm) for 30 min on each side.

Thin Film Processing. A mixture of water (0.21 g), HCl 1N (0.021 g), and THF (2 g) was added dropwise to a solution of the organotin precursor (0.081 g) in anhydrous THF (2 g). The resulting solution (5 drops) was immediately spin-coated (ramp, 0.125 s; rotation speed, 1000 round/min) for 10 s. After drying in air for 15 min, the layers were treated at 120 °C for 1 h. The hybrid layer was then treated under UV-irradiation (Philips HPL-N lamp, 125 W)[65,66] or calcined at 500 or 600 °C in air for 4 h.[67] The films are hereafter labeled as TF^T, where the superscript T stand for the post-treatment used (UV or 120, 500, or 600 °C).

Thin Film Characterization. Infrared spectra were recorded in the absorption mode using a PerkinElmer Fourier transform infrared (FTIR) spectrophotometer. Contact angle measurements were performed on a Krüss DAS 100 apparatus (Drop Shape System DAS 10 Mk2) at room temperature in static mode. The results correspond to the average value of at least two measurements. The values of the polar (γ_S^p) and dispersive (γ_S^d) components of the surface energy (γ_S) were determined according to the Owens−Wendt theory using the contact angles determined for diiodomethane, ethylene glycol, and water.[68] X-ray photoelectron spectra (XPS) were recorded with a 250-XL ESCALAB from VG equipped with a Mg Kα (1253.6 eV) X-ray source. Surface charging was corrected by referencing the spectra to C−C state of the C 1s peak at binding energy at 284.6 eV. The X-ray diffraction (XRD) and the grazing incidence X-ray diffraction (GIXD) investigations were performed with a Seifert PTS 3003 diffractometer using a Cu anode and an X-ray mirror on the primary side. On the secondary side, a long soller slit and a graphite Monochromator was used. Scanning electron microscopy (SEM) images were recorded with a JEOL JSM-6700F microscope, whereas the atomic force microscopy (AFM) studies were performed using the tapping mode (Asylum research MFP-3D). The root-mean-square (rms) roughness was obtained by calculating the root-mean-square average of the roughness profile ordinates from the AFM images.

Gas Sensing Tests. The SnO_2-based films were then processed on suitable substrates to investigate their sensing characteristics. The dc electrical measurements were performed to monitor the sensor response to H_2 (500, 1000, 2500, 5000, 10 000 ppm) and CO (20, 50, 100, 200 ppm) in dry N_2 atmosphere. The sensor signal (S) is given as the resistance ratio R_{N_2}/R_{gas}, where R_{gas} and R_{N_2} denote the

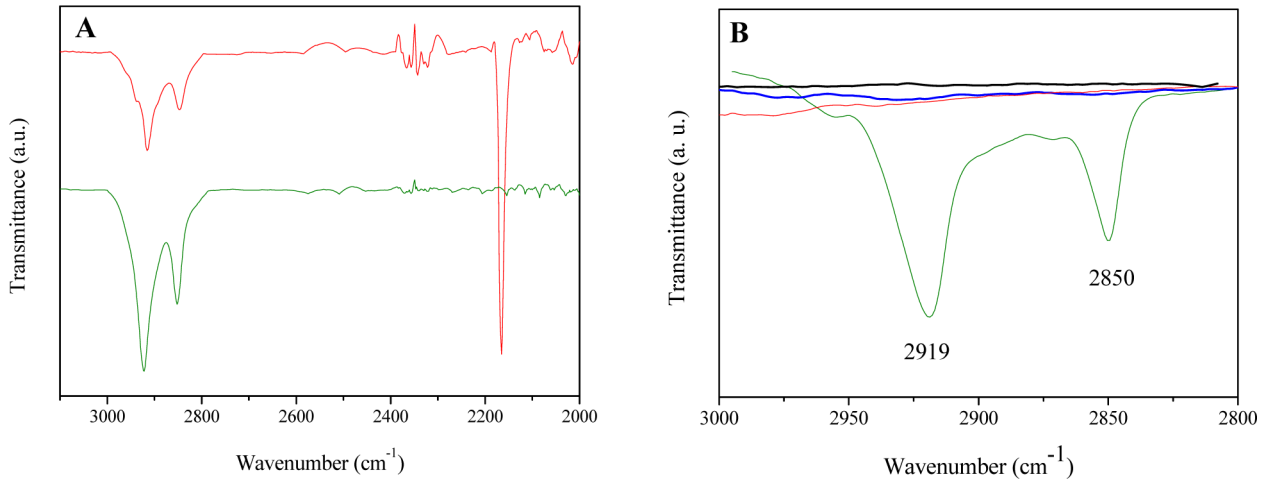

Figure 1. (A) FTIR spectra of (red) the thin film just after coating and (green) TF^{120}. (B) FTIR spectra (CH_2 stretching mode region) of (green) TF^{120}, (black) TF^{UV}, (blue) TF^{500}, and (red) TF^{600}.

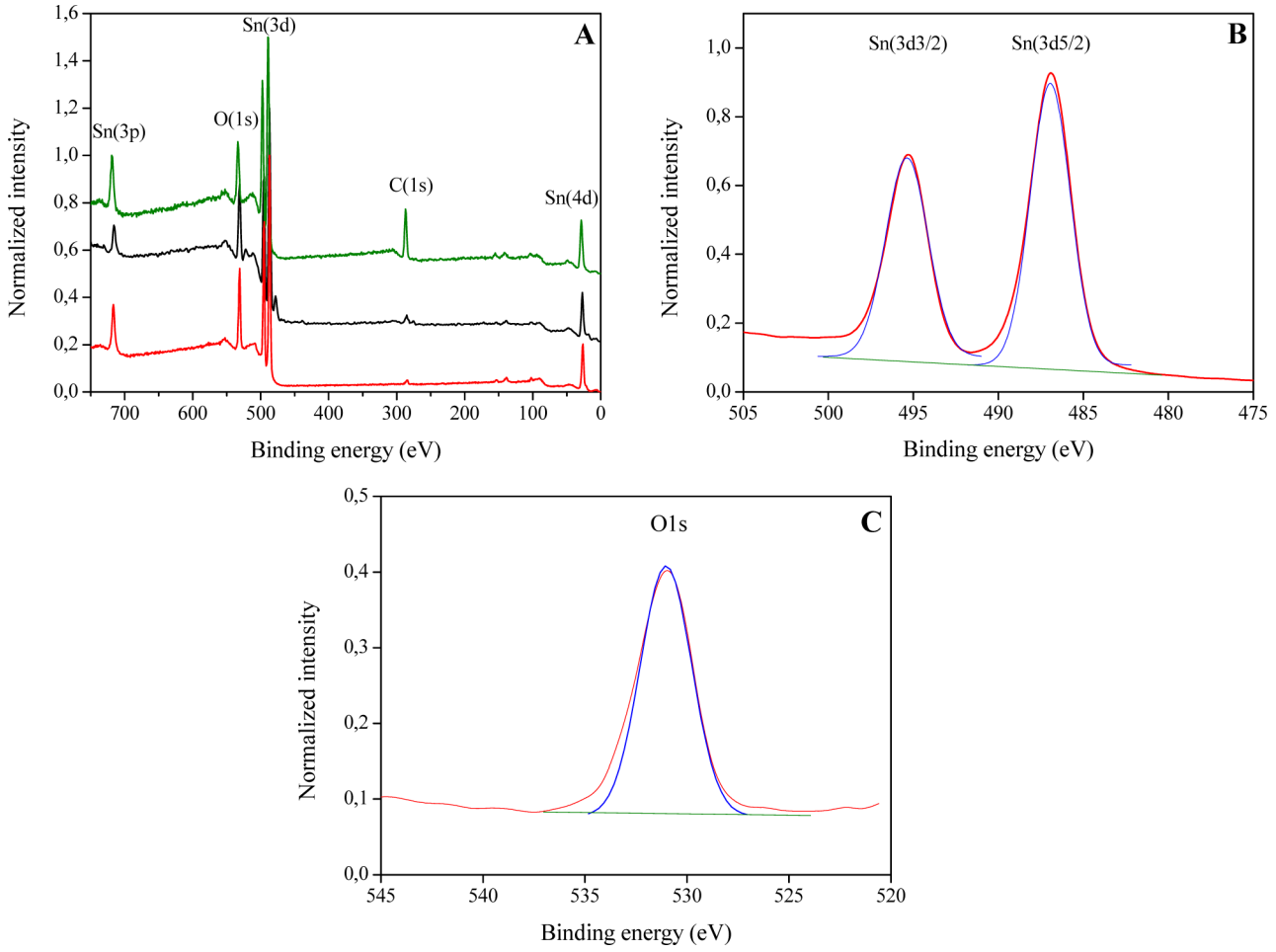

Figure 2. XPS patterns of the as-synthesized thin films. (A) XPS full survey spectra of (green) TF^{120}, (black) TF^{UV}, and (red) TF^{600}; (B) Sn 3d spectrum of TF^{600}; and (C) O 1s spectrum of TF^{600}. Peak fits are plotted in blue.

sensors' resistances with and without the presence of an analyte gas in nitrogen gas carrier, respectively.

RESULTS AND DISCUSSION

Organotin-Based Thin Film Characterization. Spin-coating from a sol containing the organotin precursor yielded tin-based hybrid layers (TF^{120}). As evidenced by the collapse of the 2169 cm^{-1} band assigned to the triple bond stretching vibration of propynyl groups (FTIR), aging at 120 °C for 1 h was required for achieving the complete hydrolysis of 1,4-bis(triprop-1-ynylstannyl)butane. Moreover, two rather sharp resonances were detected for TF^{120} at 2850 and 2919 cm^{-1} that can be assigned to the symmetric and asymmetric CH_2 stretching vibration modes (Figure 1). The energies of the

dx.doi.org/10.1021/am504723t | ACS Appl. Mater. Interfaces 2014, 6, 17093−17101

methylene vibrations are known to be a good probe of the conformation and the local organization of the alkyl chains.[69] In self-assembled alkyl monolayers,[70,71] these bands were thus found in the ranges of 2851−2849 and 2921−2917 cm^{-1} that was typical of fully extended all-trans alkyl chains.[72] As a consequence, the butylene linker within the TF^{120} layer showed a close packing with a weak population of the gauche conformers.

On the other hand, solid-state NMR experiments performed on powders obtained through similar hydrolysis conditions revealed that the tin−carbon bond has remained unaffected upon hydrolysis. Indeed, a single pattern of isotropic band located at 465 ppm was detected by solid-state ^{119}Sn NMR that could be easily attributed to six-coordinated oxo-hydroxo monoalkyltin sites according to literature data concerning oxo-hydroxo monobutyltin clusters.[73] In addition, only the characteristic features of Sn, O, and C atoms were observed by XPS for TF^{120}, the important contribution of the C 1s component accounting for the presence of the organic linker in the film (Figure 2A).

The hybrid nature of TF^{120} was also assessed by its surface properties. Thus, the total surface energy (γ_S) was found to be 32.3 ± 0.3 $mJ{\cdot}m^{-2}$ with polar (γ_S^p) and dispersive (γ_S^d) components of 4.6 ± 0.1 and 27.6 ± 0.2 $mJ{\cdot}m^{-2}$, respectively. These values were consistent with those reported for silsesquioxane-based polymer nanocomposites using the nano-building block approach.[74] Furthermore, XRD (Figure 3a) and

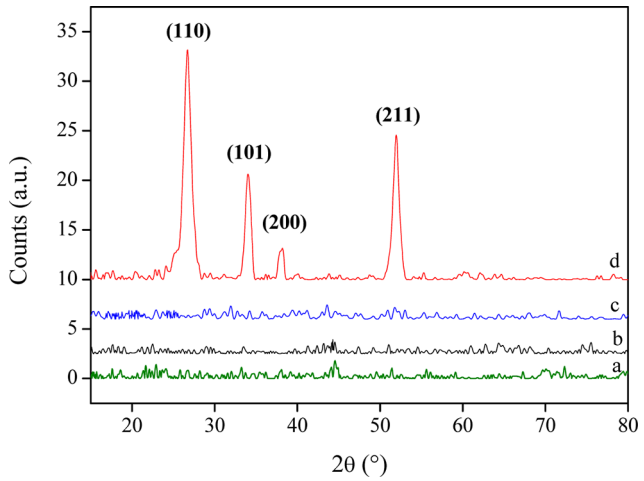

Figure 3. X-ray diffraction patterns of (a, green) TF^{120}, (b, black) TF^{UV}, (c, blue) TF^{500}, and (d, red) TF^{600}.

AFM (not shown) studies revealed that TF^{120} was amorphous and made of aggregated hybrid particles as previously found for similar layer including a decylene spacer.[63] As a result, the hydrolysis−condensation process was achieved, leading to the formation of an organotin-based hybrid layer with a local organization of the butylene spacer as reported for the bulk materials including longer alkyl chains.[75]

Tin Oxide-Based Thin Film Characterization. Previous studies have shown that, on one hand, a calcination at a temperature higher than 450 °C was necessary to remove completely the butylene linker (according to FTIR and thermogravimetry coupled to mass spectrometry analyses),[67] and on the other hand, photochemical calcination was an efficient method to produce nanocrystalline porous oxide layers,[76,77] but the as-prepared TF^{120} hybrid films were either annealed at 500−600 °C or treated under UV-irradiation in air to get tin oxide films. Regardless of the post-treatment used, the FTIR spectra revealed the elimination of the butylene linker, as evidenced by the disappearance of the stretching CH_2 vibration bands (Figure 1B). If this trend was expected for calcination above 500 °C, it is worth mentioning that a simple UV treatment in air for 4 h was also sufficient to decompose a saturated organic unit as the butylene spacer. The post-treatment also had a strong influence on the surface properties of the films. Thus, the water contact angle has drastically decreased from 71.1 ± 0.1° for TF^{120} to less than 5° for post-treated layers, while diiodomethane contact angles of 46.5 ± 1.4°, 49.9 ± 1.8°, and 52.5 ± 2.0° were measured for TF^{UV}, TF^{500}, and TF^{600}, respectively. As a result, very hydrophilic surfaces were formed upon post-treatment that might be rationalized by postulating the presence of surface hydroxyl groups in TF^{UV}, TF^{500}, and TF^{600}. To get deeper insights in the surface structure of the thin films prepared, XPS studies were carried out and the corresponding experimental data are shown in Figure 2 and Table 2. In Figure 2A, all of the features were

Table 2. Binding Energy As Revealed by X-ray Photoelectron Spectroscopy

sample	Sn $3d_{5/2}$ (eV)	Sn $3d_{5/2}$ (eV)	O 1s (eV)	C 1s (eV)
TF^{500}	486.6	495.0	530.5	284.6
TF^{600}	486.7	495.1	530.7	284.6
TF^{UV}	486.9	495.2	531.1	284.8

ascribed to Sn, O, and C elements, and no additional peaks of other atoms were detected. Upon annealing at high temperature, the C 1s peak has dramatically collapsed, and the residual carbon (284.6 eV) peak corresponds to carbon contamination. Furthermore, two symmetric peaks located at 486.6 ± 0.1 and 495.1 ± 0.1 eV were observed for TF^{500} and TF^{600} and were assigned to the Sn $3d_{5/2}$ and Sn $3d_{3/2}$ bands. The Sn $3d_{5/2}$ region exhibited a single feature at a binding energy of 486.6 ± 0.1 eV, confirming that the sample was composed of only Sn (IV) states,[78] with no noticeable Sn (II), which was expected at 485.8 eV, nor Sn(0), which was at 484.5 eV.[79] Spin−orbit coupling of the 3d state gave rise to two peaks with a spin−orbit separation of 8.5 ± 0.1 eV, which matches very well with that expected for SnO_2. In addition, the main feature in the O 1s region (Figure 2C) was located at 530.7 eV for both calcined samples and was attributed to the lattice oxygen O^{2-}, confirming the formation of a metal oxide. As far as the UV-treated film is concerned, the conclusions were similar even though the peaks were slightly shifted toward higher energies. In particular, the O 1s peak for TF^{UV} was found to be at higher binding energy than for the annealed samples, indicating the presence of more surface hydroxyl groups or oxygen−carbon bonds. Moreover, the carbon content was higher than that for the calcined films. As a result, photocalcination has clearly induced the decomposition of the butylene spacer ,leading to the formation of tin oxide, but some carbon amounts still remained on the film surface.

For treatment below 600 °C, no diffraction peaks were observed, revealing amorphous or very poorly crystallized film structures (Figure 3). In contrast, several reflection peaks were recorded for TF^{600} that could be readily indexed to the pure tetragonal phase of SnO_2, that is, cassiterite (JCPDS Card No. 41-1445). The mean crystallite size was estimated to be 9.0 ± 0.5 nm from the half-width of the {110} diffraction line using

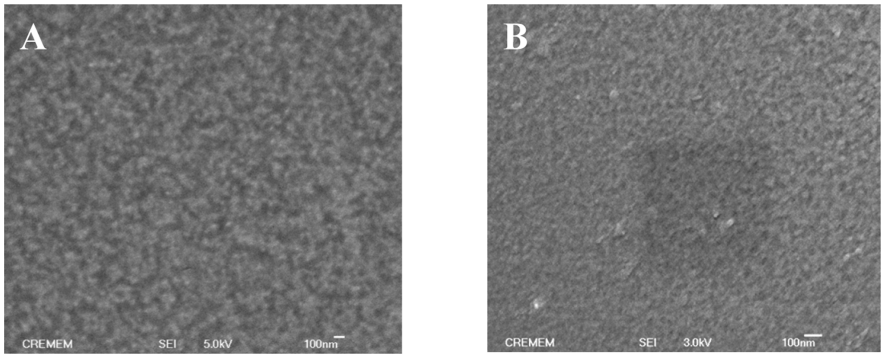

Figure 4. SEM images of (A) TF^{500} and (B) TF^{600}.

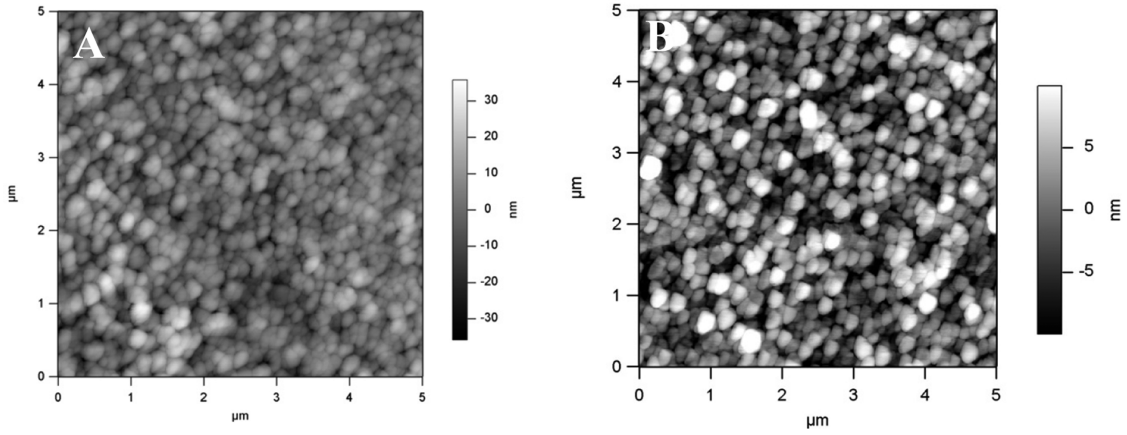

Figure 5. AFM images of (A) TF^{UV} and (B) TF^{500} or TF^{600}.

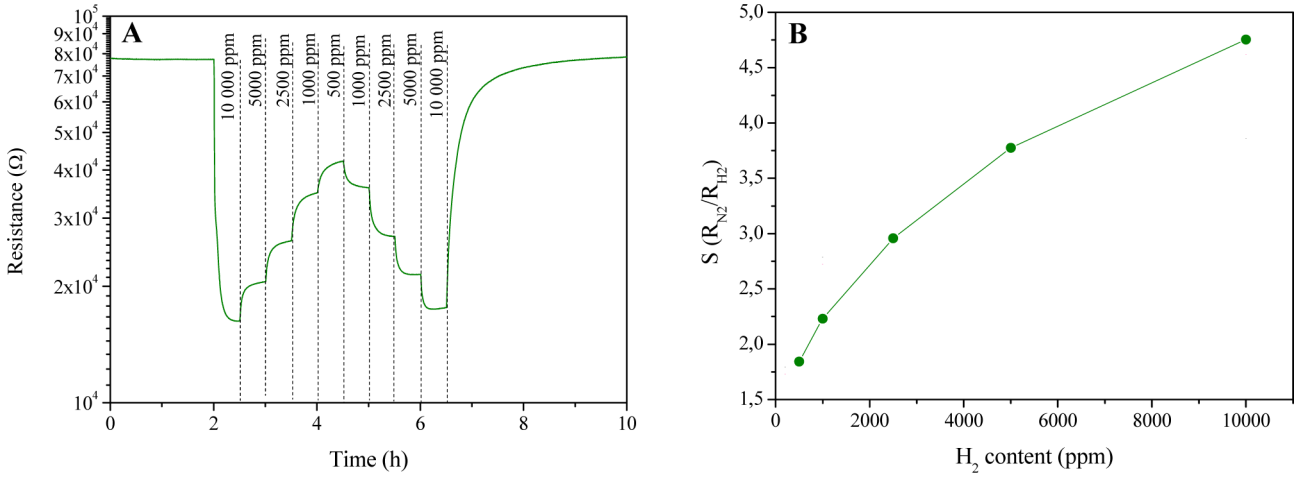

Figure 6. (A) Transient response toward H_2 in N_2 atmosphere at 150 °C for TF^{120} film and (B) calibration curve to H_2 at 150 °C.

the Scherrer equation.[80] The SEM images of annealed thin films showed a smooth and rather dense surface with a worm-hole-like porous texture. Some small particles could be observed, the size of which was about 100 nm (Figure 4).

Figure 5 depicts the surface topography of the oxide layers on glass substrate obtained after both UV and thermal treatments of the butylene-based hybrid films. AFM images recorded in the tapping mode revealed the formation of films made of a network of aggregated particles, the size of which is between 100 and 200 nm, which is consistent with the SEM images shown in Figure 4. The rms roughness of the layers annealed at high temperature was about 5 nm, and the UV-treatment led to denser and rougher surfaces (i.e., rms roughness around 10 nm). As a result, the surface topography of the post-treated films was similar, whichever treatment was used, and the UV treatment yielded a denser packing and rougher surface. It is also worth mentioning that these surfaces are rather rough, as expected for nanoparticulate films, in comparison with organosilane self-assembled monolayers on silica substrates, the rms roughness of which is less than 1 nm.[81]

Gas Sensing Properties. The TF^{120} films, which are thermally stable up to 250 °C, are sensitive toward H_2 and do not show any signals toward CO in the N_2 atmosphere at 50–

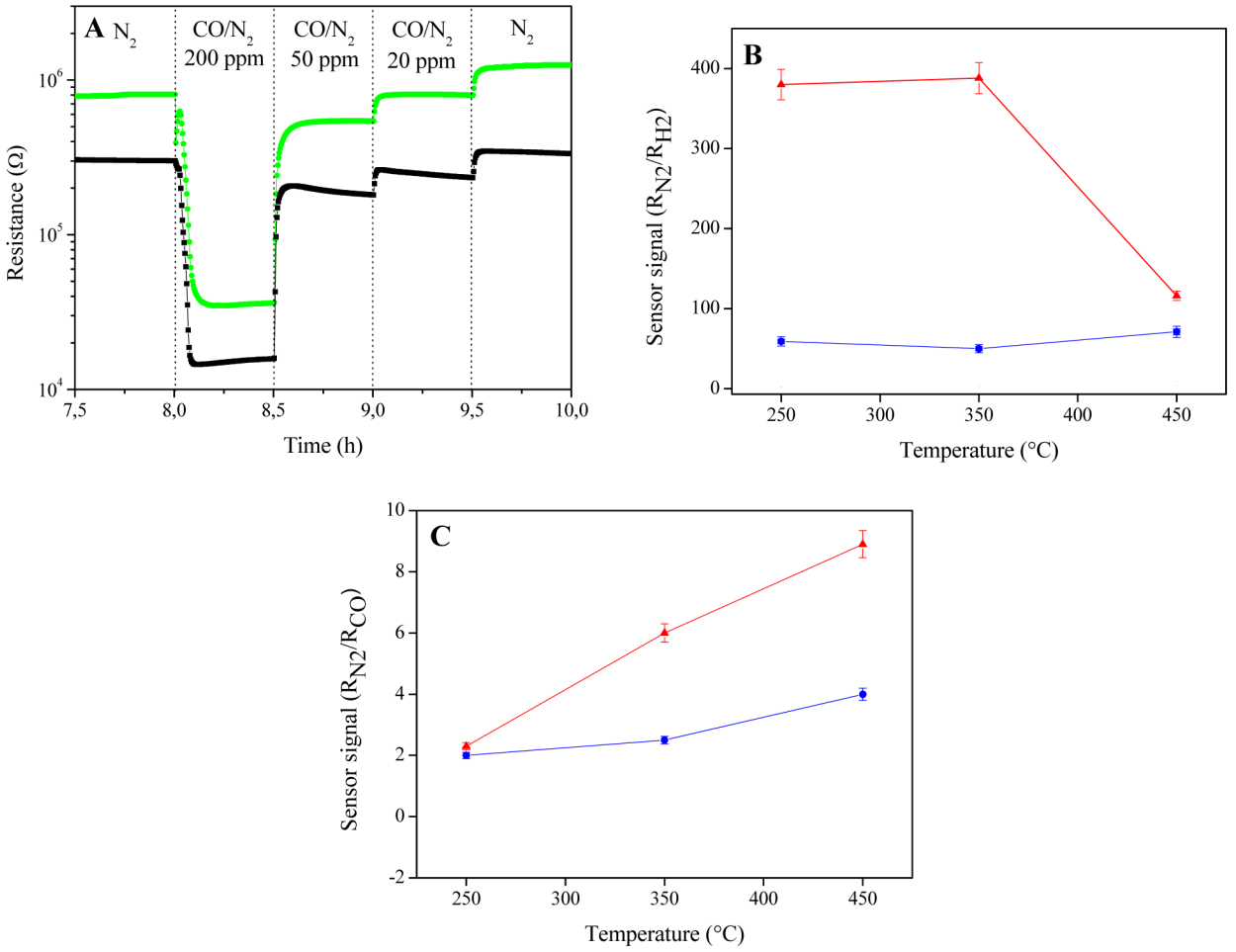

Figure 7. (A) Transient response toward CO in N_2 atmosphere at (green) 350 and (black) 450 °C for TF^{600}. (B and C) Sensor signals of (blue ●) TF^{500} and (red ▲) TF^{600} films toward (B) 1000 ppm of H_2 and (C) 200 ppm of CO.

250 °C (Figure 6A). The sensor signals vary from 1.7 to 4.6 and from 500 to 10 000 ppm, respectively (Figure 6B).

These sensor signals are remarkable and comparable with, for instance, those reported for SnO_2 nanowires.[82] Moreover, detection of H_2 at low temperature with SnO_2-based materials usually requires doping with noble metals such as platinum.[83,84] Thus, the hybrid TF^{120} films demonstrate good selectivity toward low H_2 concentrations which is in good agreement with the results recently reported for similar hybrid thin films.[63]

The gas-sensing properties of the post-treated films are rather different. The TF^{UV} films are not sensitive to H_2 and CO at the concentrations and operating temperatures under study, whereas the calcined TF^{600} films yielded responses to H_2 and CO at 250−450 °C.

For instance, Figure 7A displays the transient response of the TF^{600} films to low CO concentrations (<200 ppm) at 350 and 450 °C. The sensor signal to 200 ppm of CO is about 22 and 20 at 350 and 450 °C, respectively. TF^{600} films display a similar response to H_2, reaching sensor signals about 400 to 1000 ppm at 350 °C. Finally, the best operating temperature for both CO and H_2 was around 350 °C. In contrast, the TF^{500} films are rather insensitive to CO and H_2, displaying sensor signals of about 2 at 250 °C and 4 at 450 °C to CO (200 ppm) and about 59 at 250 °C and 71 at 450 °C to H_2 (1000 ppm). Both TF^{500} and TF^{600} films recover their initial resistance carrier gas (N_2) after being exposed to H_2 and CO, thus indicating the reversibility of the interaction between target gas molecules and SnO_2.

It is worth mentioning that the gas sensing properties of metal oxides are generally considered to depend mainly on the size of SnO_2 crystallites and the porosity of SnO_2 layers.[85] As the textural properties of TF^{500} and TF^{600} were quite similar, the difference in gas sensing properties of the hybrid layers calcined at 500 and 600 °C can therefore be easily rationalized by comparing the crystallinity of both layers. Indeed, according to the results of the XRD characterization, the TF^{600} film is made of SnO_2 nanocrystallites of about 9 nm in diameter, whereas the TF^{500} film is amorphous. This is therefore fully consistent with the fact that the detection of reducing gases strongly depends upon the crystallinity of SnO_2. Therefore, the films calcined at 600 °C and composed of nanocrystalline cassiterite SnO_2 particles demonstrate good response to H_2, displaying sensors signals of about 400−1000 ppm of H_2 at 300−350 °C. These values are comparable those reported for monodispersed (3.5 nm) SnO_2 nanocrystals synthesized by a liquid route,[32] and higher than those (~25) reported for mesostructured SnO_2 prepared by the template route,[86] and those (~50) for macroporous SnO_2 films prepared using PMMA microspheres.[87] The response of the TF^{600} films to 200 ppm of CO is comparable to that reported for SnO_2 opals and inverse-opals microstructures, that is, of about 22 at 350 °C and about 10 at 400 °C,[88] respectively, and is significantly lower

than that found for monodispersed (3.5 nm) SnO_2 nanocrystals (150 at 300 °C).[32]

CONCLUSION

Tin dioxide thin layers were prepared by UV-treatment or calcination at 500 and 600 °C of organotin-based hybrid thin films. Regardless of the post-treatment nature, the complete elimination of the organic spacer present in the hybrid layers was evidenced by FTIR and XPS spectroscopies, leading to films composed of a network of aggregated particles. However, only a thermal treatment at 600 °C yielded the formation of cassiterite nanocrystalline SnO_2 particles, according to XRD characterization. Both hybrid and tin dioxide thin films were used as gas sensing materials for the detection of CO and H_2. The best selectivity to H_2 was observed at 150 °C with hybrid thin films that do not display any response to CO at 20−200 °C. To the best of our knowledge, this constitutes one of the rare examples of gas sensing properties of an organic−inorganic hybrid layer. The SnO_2 films obtained by calcinations of the previous hybrid layer at 600 °C are more sensitive to H_2 than to CO, as is usually observed for SnO_2-sensors, and their best operating temperature is in the 300−350 °C range. The sensor signals measured for these films fall within the range of those reported for SnO_2-based nanostructures. which validates the approach developed in this work.

AUTHOR INFORMATION

Corresponding Author

*Tel: 33 (0)5 40 00 25 23. E-mail: t.toupance@ism.u-bordeaux1.fr.

Funding

This work was supported by the MENRT (LR fellowship), the CNRS, the Aquitaine Region (Contract no. 09002556) and the European Community (FAME Network of Excellence). It was carried out within the framework of EMMI (European Multifunctional Material Institute).

Notes

The authors declare no competing financial interest.

ACKNOWLEDGMENTS

We thank Dr. François Ribot and Dr. Elisabeth Sellier for their valuable assistance with solid-state CP-MAS NMR and HR-SEM measurements.

REFERENCES

(1) Hagemeyer, A.; Hogan, Z.; Schlichter, M.; Smaka, B.; Streukens, G.; Turner, H.; Volpe, A., Jr.; Weinberg, H.; Yaccato, K. High Surface Area Tin Oxide. *Appl. Catal., A* **2007**, *317*, 139−148.

(2) Kamiuchi, N.; Mitsui, T.; Yamaguchi, N.; Muroyama, H.; Matsui, T.; Kikuchi, R.; Eguchi, K. Activation of Pt/SnO_2 Catalyst for Catalytic Oxidation of Volatile Organic Compounds. *Catal. Today* **2010**, *157*, 415−419.

(3) Wu, S.; Cao, H.; Yiu, S.; Liu, X.; Zhang, X. Amino Acid-Assisted Hydrothermal Synthesis and Photocatalysis of SnO_2 Nanocrystals. *J. Phys. Chem. C* **2009**, *113*, 17893−1898.

(4) Kumar, V.; Govind, A.; Nagarajan, R. Optical and Photocatalytic Properties of Heavily F^--doped SnO_2 Nanocrystals by a Novel Single-source Precursor Approach. *Inorg. Chem.* **2011**, *50*, 5637−5645.

(5) Chopra, K. L.; Major, S.; Pandya, D. K. Transparent Conductors-A Status Review. *Thin Solid Films* **1983**, *102*, 1−46.

(6) Mubeen, S.; Moskovits, M. Gate-Tunable Surface Processes on a Single-Nanowire Field-Effect Transistor. *Adv. Mater.* **2011**, *23*, 2306−2312.

(7) Shin, G.; Yoon, C. H.; Bae, M. Y.; Kim, Y. C.; Hong, S. K.; Rogers, J. A.; Ha, J. S. Stretchable Field-Effect-Transistor Array of Suspended SnO_2 Nanowires. *Small* **2011**, *7*, 1181−1185.

(8) Ha, H.-W.; Kim, K.; de Borniol, M.; Toupance, T. Fluorine-Doped Nanocrystalline SnO_2 Powders Prepared via Single Molecular Precursor Method as Anode Materials for Li-ion Batteries. *J. Solid. State Chem.* **2006**, *179*, 702−707.

(9) Chen, J. S. X.; Lou, W. D. SnO_2-based Nanomaterials: Synthesis and Application in Lithium-Ion Batteries. *Small* **2013**, *9*, 1877−1893.

(10) Subramanian, V.; Burke, W. W.; Zhu, H.; Wei, B. Novel Microwave Synthesis of Nanocrystalline SnO_2 and its Electrochemical Properties. *J. Phys. Chem. C* **2008**, *112*, 4550−4556.

(11) Selvan, R. K.; Perelshtein, I.; Perkas, N.; Gedanken, A. Synthesis of Hexagonal-Shaped SnO_2 Nanocrystals and SnO_2@C Nanocomposites for Electrochemical Redox Supercapacitors. *J. Phys. Chem. C* **2008**, *112*, 1825−1830.

(12) Wang, C.; Zhou, Y.; Ge, M.; Xu, X.; Zhang, Z.; Jiang, J. Z. Large-Scale Synthesis of SnO_2 Nanosheets with High Lithium Storage Capacity. *J. Am. Chem. Soc.* **2009**, *132*, 46−47.

(13) Gubbala, S.; Chakrapani, V.; Kumar, V.; Sunkara, M. K. Band-Edge Engineered Hybrid Structures for Dye-Sensitized Solar Cells Based on SnO_2 Nanowires. *Adv. Funct. Mater.* **2008**, *18*, 2411−2418.

(14) Birkel, A.; Lee, Y.-G.; Koll, D.; Van Meerbeek, X.; Frank, S.; Choi, M. J.; Kang, Y. S.; Char, K.; Tremel, W. Highly Efficient and Stable Dye-Sensitized Solar Cells Based on SnO_2 Nanocrystals Prepared by Microwave-Assisted Synthesis. *Energy Environ. Sci.* **2012**, *5*, 5392−5400.

(15) Cojocaru, L.; Olivier, C.; Toupance, T.; Sellier, E.; Hirsch, L. Size and Shape Fine-tuning of SnO_2 Nanoparticles for Highly Efficient and stable dye-sensitized Solar Cells. *J. Mater. Chem. A* **2013**, *1*, 13789−13799.

(16) Barsan, N.; Schweizer-Berberich, M.; Göpel, W. Fundamental and Practical Aspects in the Design of Nanoscaled SnO_2 Gas Sensors: A Status Report. *Fresenius J. Anal. Chem.* **1999**, *365*, 287−304.

(17) Sahm, T.; Gurlo, A.; Barsan, N.; Weimar, U.; Madler, L. Fundamental Studies on SnO_2 by Means of Simultaneous Work Function Change and Conduction Measurements. *Thin Solid Films* **2005**, *490*, 43−46.

(18) Graf, M.; Gurlo, A.; Barsan, N.; Weimar, U.; Hierlemann, A. Microfabricated Gas Sensor Systems with Sensitive Nanocrystalline Metal-oxide Films. *J. Nanopart. Res.* **2006**, *8*, 823−839.

(19) Gardon, M.; Guilemany, M. A Review on Fabrication, Sensing Mechanisms and Performance of Metal Oxide Gas Sensors. *J. Mater. Sci.: Mater. Electron.* **2013**, *24*, 1410−1421.

(20) Barsan, N.; Koziej, D.; Weimar, U. Metal Oxide-based Gas Sensor Research: How to? *Sens. Actuators, B* **2007**, *121*, 18−35.

(21) Gurlo, A. Interplay between O_2 and SnO_2: Oxygen Ionosorption and Spectroscopic Evidence for Adsorbed Oxygen. *ChemPhysChem* **2006**, *7*, 2041−2052.

(22) Gurlo, A.; Riedel, R. In Situ and Operando Spectroscopy for Assessing Mechanisms of Gas Sensing. *Angew. Chem., Int. Ed.* **2007**, *46*, 3826−3848.

(23) D'Arienzo, M.; Cristofori, D.; Scotti, R.; Morazzoni, F. New Insights into the SnO_2 Sensing Mechanism Based on the Properties of Shape Controlled Tin Oxide Nanoparticles. *Chem. Mater.* **2013**, *25*, 3675−3686.

(24) Wang, Z. L. Nanobelts, Nanowires, and Nanodiskettes of Semiconducting Oxides—From Materials to Nanodevices. *Adv. Mater.* **2003**, *15*, 432−436.

(25) Kolmakov, A.; Zhang, Y.; Cheng, G.; Moskovits, M. Detection of CO and O_2 Using Tin Oxide Nanowire Sensors. *Adv. Mater.* **2003**, *15*, 997−1000.

(26) Li, L.-L.; Zhang, W.-M.; Yuan, Q.; Li, Z.-X.; Fang, C.-J.; Sun, L.-D.; Wan, L.-J.; Yan, C.-H. Room Temperature Ionic Liquids Assisted Green Synthesis of Nanocrystalline Porous SnO_2 and their Gas Sensor Behaviors. *Cryst. Growth Des.* **2008**, *8*, 4165−4171.

(27) Han, C. H.; Han, S.-D.; Singh, I.; Toupance, T. Micro-Bead of Nano-Crystalline F-doped SnO_2 as a Sensitive Hydrogen Gas Sensor. *Sens. Actuators, B* **2005**, *109*, 264−269.

(28) Mosadegh Sedghi, S.; Mortazavi, Y.; Khodadadi, A. Low Temperature CO and CH_4 Dual Selective Gas Sensor Using SnO_2 Quantum Dots Prepared by Sonochemical Method. *Sens. Actuators, B* **2010**, *145*, 7−12.
(29) Chiu, H.-C.; Yeh, C.-S. Hydrothermal Synthesis of SnO_2 Nanoparticles and their Gas-Sensing of Alcohol. *J. Phys. Chem. C* **2007**, *111*, 7256−7259.
(30) Pinna, N.; Neri, G.; Antonietti, M.; Niederberger, M. Nonaqueous Synthesis of Nanocrystalline Semiconducting Metal Oxides for Gas Sensing. *Angew. Chem., Int. Ed.* **2004**, *43*, 4345−4349.
(31) Nayral, C.; Ould-Ely, T.; Maisonnat, A.; Chaudret, B.; Fau, P.; Lescouzères, L.; Peyre-Lavigne, A. A Novel Mechanism for the Synthesis of Tin/Tin Oxide Nanoparticles of Low Size Dispersion of Nanostructured SnO_2 for the Sensitive Layers of Gas Sensors. *Adv. Mater.* **1999**, *11*, 61−63.
(32) Kida, T.; Doi, T.; Shimanoe, K. Synthesis of Monodispersed SnO_2 Nanocrystals and their Remarkably High Sensitivity to Volatile Organic Compounds. *Chem. Mater.* **2010**, *22*, 2662−2667.
(33) Aboulaich, A.; Boury, B.; Mutin, P. H. Reactive and Organosoluble SnO_2 Nanoparticles by a Surfactant-free Non-Hydrolytic Sol−Gel Route. *Eur. J. Inorg. Chem.* **2011**, 3644−3649.
(34) Huang, H.; Lee, Y. C.; Tan, O. K.; Zhou, W.; Peng, N.; Zhang, Q. High Sensitivity SnO_2 Single-Nanorod Sensors for the Detection of H_2 Gas at Low Temperature. *Nanotechnology* **2009**, *20*, 115501.
(35) Liu, J.; Gu, F.; Hu, Y.; Li, C. Flame Synthesis of Tin Oxide Nanorods: A Continuous and Scalable Approach. *J. Phys. Chem. C* **2010**, *114*, 5867−5870.
(36) Cao, H.; Qiu, X.; Liang, Y.; Zhang, L.; Zhao, M.; Zhu, Q. Sol−Gel Template Synthesis and Photoluminescence of n- and p-Type Semiconductor Oxide Nanowires. *ChemPhysChem* **2006**, *7*, 497−500.
(37) Kuang, Q.; Lao, C.; Wang, Z. L.; Xie, Z.; Zheng, L. High-Sensitivity Humidity Sensor Based on a Single SnO_2 Nanowire. *J. Am. Chem. Soc.* **2007**, *129*, 6070−6071.
(38) Feng, H.; Huang, J.; Li, J. A Mechanical Actuated SnO_2 Nanowire for Small Molecules Sensing. *Chem. Commun.* **2013**, *49*, 1017−1019.
(39) Yang, R.; Wang, Z. L. Springs, Rings, and Spirals of Rutile-Structured Tin Oxide Nanobelts. *J. Am. Chem. Soc.* **2006**, *128*, 1466−1467.
(40) Liu, Y.; Dong, J.; Liu, M. Well-Aligned "Nano-Box-Beams" of SnO_2. *Adv. Mater.* **2004**, *16*, 353−356.
(41) Wang, Z.; Luan, D.; Boey, F. Y. C.; Lou, X. W. Fast Formation of SnO_2 Nanoboxes with Enhanced Lithium Storage Capability. *J. Am. Chem. Soc.* **2011**, *133*, 4738−4741.
(42) Jiang, L. Y.; Xu, X. L.; Guo, Y. G.; Wan, L. J. SnO_2-Based Hierarchical Nanomicrostructures: Facile Synthesis and Their Applications in Gas Sensors and Lithium-Ion Batteries. *J. Phys. Chem. C* **2009**, *113*, 14213−14219.
(43) Gyger, F.; Hübner, M.; Feldmann, C.; Barsan, N.; Weimar, U. Nanoscale SnO_2 Spheres and Their Application as a Gas-sensing Material. *Chem. Mater.* **2010**, *22*, 4821−4827.
(44) Sutti, A.; Baratto, C.; Calestani, G.; Dionigi, C.; Ferroni, M.; Faglia, G.; Sberveglieri, G. Inverse Opal Gas Sensors: Zn(II)-Doped Tin Dioxide Systems for Low Temperature Detection of Pollutant Gases. *Sens. Actuators, B* **2008**, *130*, 567−573.
(45) D'Arienzo, M.; Armelao, L.; Cacciamani, A.; Mari, C. M.; Polizzi, S.; Ruffo, R.; Scotti, R.; Testino, A.; Wahba, L.; Morazzoni, F. One-Step Preparation of SnO_2 and Pt-Doped SnO_2 as Inverse Opal Thin Films for Gas Sensing. *Chem. Mater.* **2010**, *22*, 4083−4089.
(46) Wagner, T.; Haffer, S.; Weinberger, C.; Klaus, D.; Tiemann, M. Mesoporous Materials as Gas Sensors. *Chem. Soc. Rev.* **2013**, *42*, 4036−4053.
(47) Han, X.; Jin, M.; Xie, S.; Kuang, Q.; Jiang, Z.; Jiang, Y.; Xie, Z.; Sheng, L. Synthesis of Tin Dioxide Octahedral Nanoparticles with Exposed High-Energy {221} Facets and Enhanced Gas-Sensing Properties. *Angew. Chem., Int. Ed.* **2009**, *48*, 9180−9183.
(48) Gurlo, A. Nanosensors: Towards Morphological Control of Gas Sensing Activity. SnO_2, In_2O_3, ZnO, and WO_3 Case Studies. *Nanoscale* **2011**, *3*, 154−165.
(49) Wang, X.; Han, X.; Xie, S.; Kuang, Q.; Jiang, Y.; Zhang, S.; Mu, X.; Chen, G.; Xie, Z.; Zheng, L. Controlled Synthesis and Enhanced Catalytic and Gas-Sensing Properties of Tin Dioxide Nanoparticles with Exposed High-Energy Facets. *Chem.—Eur. J.* **2012**, *18*, 2283−2289.
(50) Wang, H.; Dou, H.; Teoh, W. Y.; Zhan, Y.; Hung, T. F.; Zhang, F.; Xu, J.; Zhang, R.; Rogach, A. L. Engineering of Facets, Band Structure, and Gas-Sensing Properties of Hierarchical Sn^{2+}-Doped SnO_2 Nanostructures. *Adv. Funct. Mater.* **2013**, *23*, 4847−4853.
(51) Serventi, A. M.; Rickerby, D. G.; Horrillo, M. C.; Saint-Jacques, R. G. Transmission Electron Microscopy Investigation of the Effect of Deposition Conditions and a Platinum Layer in Gas-Sensitive r.f.-Sputtered SnO_2 Films. *Thin Solid Films* **2003**, *445*, 38−47.
(52) Shen, Y.; Yamazaki, T.; Liu, Z.; Jin, C.; Kikuta, T.; Nakatani, N. Porous SnO_2 Sputtered Films with High H_2 Sensitivity at Low Operation Temperature. *Thin Solid Films* **2008**, *516*, 5111−5117.
(53) Pan, S. S.; Ye, C.; Teng, X. M.; Fan, H. T.; C. H, Li Localized Exciton Luminescence in Nitrogen-Incorporated SnO_2 Thin Films. *Appl. Phys. A: Mater. Sci. Process.* **2006**, *85*, 251911.
(54) Sundqvist, J.; Lu, J.; Ottosson, M.; Harsta, A. Growth of SnO_2 Thin Films by Atomic Layer Deposition and Chemical Vapour Deposition: A Comparative Study. *Thin Solid Films* **2006**, *514*, 63−68.
(55) Zhao, J.; Wu, S.; Liu, J.; Liu, H.; Gong, S.; Zhou, D. Tin Oxide Thin Films Prepared by Aerosol-Assisted Chemical Vapor Deposition and the Characteristics on Gas Detection. *Sens. Actuators, B* **2010**, *145*, 788−793.
(56) Bruneaux, J.; Cachet, H.; Froment, M.; Messad, A. Correlation Between Structural and Electrical Properties of Sprayed Tin Oxide Films with and without Fluorine Doping. *Thin Solid Films* **1991**, *197*, 129−136.
(57) Enesca, A.; Duta, A. The Influence of Organic Additives on the Morphologic and Crystalline Properties of SnO_2 Obtained by Spray Pyrolysis Deposition. *Thin Solid Films* **2011**, *519*, 5780−5786.
(58) Velasquez, C.; Rojas, F.; Esparza, J. M.; Ortiz, A.; Campero, A. Physicochemical Aspects of Novel Surfactantless, Self-Templated Mesoporous SnO_2 Thin Films. *J. Phys. Chem. B* **2006**, *110*, 11832−11837.
(59) Brezesinski, T.; Fisher, A.; Iimura, K-i.; Sanchez, C.; Grosso, D.; Antonietti, M.; Smarlsy, B. M. Generation of Self-Assembled 3D Mesostructured SnO_2 Thin Films with Highly Crystalline Frameworks. *Adv. Funct. Mater.* **2006**, *16*, 1433−1440.
(60) Molloy, K. C. Precursors for the Formation of Tin(IV) Oxide and Related Materials. *J. Chem. Res.* **2008**, 549−554.
(61) Boyle, T. J.; Ward, T. L.; De'Angeli, S. M.; Xu, H.; Hammetter, W. F. Properties of MOCVD Deposits Using Novel Sn(II) Neo-Pentoxide Precursors. *Chem. Mater.* **2003**, *15*, 765−775.
(62) El Hamzaoui, H.; Jousseaume, B.; Riague, R.; Toupance, T.; Dieudonné, P.; Zakri, C.; Maugey, M.; Allouchi, H. Self-Assembled Tin-based Bridged Hybrid Materials. *J. Am. Chem. Soc.* **2004**, *126*, 8130−8131.
(63) Renard, L.; Elhamzaoui, H.; Jousseaume, B.; Toupance, T.; Laurent, G.; Ribot, F.; Saadaoui, H.; Brötz, J.; Fuess, H.; Riedel, R.; Gurlo, A. Low-Temperature H_2 Sensing in Self-Assembled Organotin Thin Films. *Chem. Commun.* **2011**, *47*, 1464−1466.
(64) Jousseaume, B.; Riague, H.; Toupance, T.; Lahcini, M.; Mountford, P.; Tyrrell, B. R. A General Route to Alkylene-, Arylene-, or Benzylene-Bridged Ditin Hexachlorides and Hexaalkynides. *Organometallics* **2002**, *21*, 4590−4594.
(65) Tebby, Z.; Babot, O.; Toupance, T.; Park, D.-H.; Campet, G.; Delville, M.-H. Low-Temperature UV-Processing of Nanocrystalline Nanoporous Thin TiO_2 Films: An Original Route toward Plastic Electrochromic Systems. *Chem. Mater.* **2008**, *20*, 7260−7267.
(66) Tebby, Z.; Uddin, T.; Nicolas, Y.; Olivier, C.; Toupance, T.; Labrugère, C.; Hirsch, L. Low-Temperature UV Processing of Nanoporous SnO_2 Layers for Dye-Sensitized Solar Cells. *ACS Appl. Mater. Interfaces* **2011**, *3*, 1485−1491.
(67) Toupance, T.; El Hamzaoui, H.; Jousseaume, B.; Riague, H.; Saadeddin, I.; Campet, G.; Brötz, J. Bridged-Polystannoxane: A New

Route toward Nanoporous Tin Dioxide. *Chem. Mater.* **2006**, *18*, 6364−6372.
(68) Owens, D. K.; Wendt, R. C. Estimation of the Surface Free Energy of Polymers. *J. Appl. Polym. Sci.* **1969**, *13*, 1741−1747.
(69) Martin, P.; Marsaudon, S.; Thomas, L.; Desbat, B.; Aimé, J.-P.; Bennetau, B. Liquid Mechanical Behavior of Mixed Monolayers of Amino and Alkyl Silanes by Atomic Force Microscopy. *Langmuir* **2005**, *21*, 6934−6943.
(70) Allara, D. L.; Parikh, A. N.; Rondelez, F. Evidence for a Unique Chain Organization in Long Chain Silane Monolayers Deposited on Two Widely Different Solid Substrates. *Langmuir* **1995**, *11*, 2357−2360.
(71) Baptiste, A.; Gibaud, A.; Bardeau, J. F.; Wen, K.; Maoz, R.; Sagiv, J.; Ocko, B. M. X-ray, Micro-Raman, and Infrared Spectroscopy Structural Characterization of Self-Assembled Multilayer Silane Films with Variable Numbers of Stacked Layers. *Langmuir* **2002**, *18*, 3916−3922.
(72) Snyder, R. G.; Strauss, H. L.; Elliger, C. A. C−H Stretching Modes and the Structure of n-Alkyl Chains. 1. Long, Disordered Chains. *J. Phys. Chem.* **1982**, *86*, 5145−5150.
(73) Banse, F.; Ribot, F.; Tolédano, P.; Maquet, J.; Sanchez, C. Hydrolysis of Monobutyltin Trialkoxides: Synthesis and Characterizations of $\{(BuSn)_{12}O_{14}(OH)_6\}(OH)_2$. *Inorg. Chem.* **1995**, *34*, 6371−6379.
(74) Mammeri, F.; Bonhomme, C.; Ribot, F.; Babonneau, F.; Dirè, S. New Monofunctional POSS and Its Utilization as Dewetting Additive in Methacrylate Based Free-Standing Films. *Chem. Mater.* **2009**, *21*, 4163−4171.
(75) Toupance, T.; de Borniol, M.; Elhamzaoui, H.; Jousseaume, B. Alkynylorganotins, Versatile Precursors of Class II Hybrid Materials. *Appl. Organomet. Chem.* **2007**, *21*, 514−520.
(76) Zhang, D.; Yoshida, T.; Oekermann, G.; Furuta, K.; Minoura, H. Room-Temperature Synthesis of Porous Nanoparticulate TiO_2 Films for Flexible Dye-Sensitized Solar Cells. *Adv. Funct. Mater.* **2006**, *16*, 1228−1234.
(77) Tebby, Z.; Babot, O.; Michau, D.; Hirsch, L.; Carlos, L.; Toupance, T. A Simple Route Toward Low-Temperature Processing of Nanoporous Thin Films Using UV-Irradiation: Application for Dye Solar Cells. *J. Photochem. Photobiol., A* **2009**, *205*, 70−76.
(78) Moulder, J. F.; Stikle, W. F.; Sobol, P. E.; Bomben, K. D. Handbook of X-Ray Photoelectron Spectroscopy, Perkin-Elmer Corp.: Eden Prairie, MN, 1992.
(79) Kwoka, M.; Ottaviano, L.; Passacantando, M.; Santucci, S.; Czempik, G.; Szuber, J. XPS Study of the Surface Chemistry of L-CVD SnO_2 Thin Films After Oxidation. *Thin Solid Films* **2005**, *490*, 36−42.
(80) The average crystallite size is calculated from the Scherrer relation $t = (0.9^*\lambda)/\beta\cos\theta$, where λ is the wavelength, ε the angular half-width of the *hkl* peak for the studied sample, and θ the Bragg angle for the chosen *hkl* reflection. Jenkins, R.; Synder, R. L. In *Introduction to X-ray Powder Diffractometry*, Winefordner, J. D., Ed., Wiley: New York, 1996; Chapter 3, pp 89−91.
(81) Ramin, M. A.; Le Bourdon, G.; Heuzé, K.; Degueil, M.; Belin, C.; Buffeteau, T.; Bennetau, B.; Vellutini, L. Functionalized Hydrogen-Bonding Self-Assembled Monolayers Grafted onto SiO_2 Substrates. *Langmuir* **2012**, *28*, 17672−17680.
(82) Wang, B.; Zhu, L. F.; Yang, Y. H.; Xu, N. S.; Yang, G. W. Fabrication of a SnO_2 Nanowire Gas Sensor and Sensor Performance for Hydrogen. *J. Phys. Chem. C* **2008**, *112*, 6643−6647.
(83) Shao, S.; Qiu, X.; He, D.; Koehn, R.; Guan, N.; Lu, X.; Bao, N.; Grimes, C. A. Low-Temperature Crystallization of Transparent, Highly Ordered Nanoporous SnO_2 Thin Films: Application to Room-Temperature Hydrogen Sensing. *Nanoscale* **2011**, *3*, 4283−4289.
(84) Russo, P. A.; Donato, N.; Leonardi, S. G.; Baek, S.; Conte, D. E.; Neri, G.; Pinna, N. Room-Temperature Hydrogen Sensing with Heteronanostructures Based on Reduced Graphene Oxide and Tin Oxide. *Angew. Chem., Int. Ed.* **2012**, *51*, 11053−11057.
(85) Vuong, D. D.; Sakai, G.; Shimanoe, K.; Yamazoe, N. Preparation of Grain-Size-Controlled Tin Oxide Sols by Hydrothermal Treatment for Thin Film Sensor Application. *Sens. Actuators, B* **2004**, *103*, 386−391.
(86) Wang, Y.; Wu, X.; Li, Y.; Zhou, Z. Mesostructured SnO_2 as Sensing Material for Gas Sensors. *Solid-State Electron.* **2004**, *48*, 627−632.
(87) Hyodo, T.; Sasahara, K.; Shimizu, Y.; Egashira, M. Preparation of Macroporous SnO_2 Films using PMMA Microspheres and Their Sensing Properties to NO_x and H_2. *Sens. Actuators, B* **2005**, *106*, 580−590.
(88) Scott, R. W. J.; Yang, S. M.; Chabanis, G.; Coombs, N.; Williams, D. E.; Ozin, G. A. Tin Dioxide Opals and Inverted Opals: Near-Ideal Microstructures for Gas Sensors. *Adv. Mater.* **2001**, *13*, 1468−1472.